ADVANCED FUNCTIONAL MATERIALS
www.afm-journal.de

Fluorine Functionalized MXene QDs for Near-Record-Efficiency $CsPbI_3$ Solar Cell with High Open-Circuit Voltage

Dongfang Xu, Tong Li, Yu Han, Xuexia He, Shaomin Yang, Yuhang Che, Jie Xu, Hong Zou, Xi Guo, Jungang Wang, Xuruo Lei, and Zhike Liu**

$CsPbI_3$ inorganic perovskites have attracted significant attention due to their desirable bandgap for tandem solar cells and excellent thermal stability. However, $CsPbI_3$ perovskite solar cells (PSCs) still exhibit low efficiency and high energy loss due to nonradiative recombination. Herein, functionalized $Ti_3C_2F_x$ quantum dots (QDs) are prepared and selected as interface passivators to enhance the performance of $CsPbI_3$ PSCs. The systematic experimental results reveal that $Ti_3C_2F_x$ QDs serve as effective passivators mainly in three aspects: 1) *p*-type $Ti_3C_2F_x$ QDs can tune the energy level of perovskite films and provide an efficient pathway for hole transfer; 2) $Ti_3C_2F_x$ QDs can effectively passivate defects and reduce interfacial nonradiative recombination, and 3) $Ti_3C_2F_x$ QDs form a barrier layer to prevent water invasion and improve the stability of $CsPbI_3$ PSCs. Consequently, the champion $CsPbI_3$ PSC with $Ti_3C_2F_x$ QDs treatment exhibits an excellent efficiency of 20.44% with a high open-circuit voltage of 1.22 V. Meanwhile, the corresponding device without encapsulation retained 93% of its initial efficiency after 600 h of storage in ambient air.

1. Introduction

After more than ten years of development, the current certified efficiency of organic–inorganic hybrid perovskite solar cells (PSCs) prepared in the laboratory has reached up to 25.8%.[1] However, volatile organic components in organic–inorganic hybrid perovskites would affect the long-term operational stability of the devices, impeding their commercialization.[2] Alternatively, $CsPbX_3$ (X = I^-, Br^-, Cl^-, or mixed) inorganic perovskites without volatile organic components are promising commercialization candidates with excellent chemical stability.[3] Among inorganic perovskites, $CsPbI_3$ with desirable bandgap (≈1.7 eV) and excellent light absorption is a promising material for high-performance single-junction or tandem solar cells.[4] Several strategies have been extensively developed to enhance the performance of $CsPbI_3$ PSCs, including precursor engineering,[5] additive engineering,[6] interface engineering,[7] etc. Recently, the power conversion efficiency (PCE) of the $CsPbI_3$ inorganic perovskites (without Br doping) increased rapidly to 20.37%.[8] However, $CsPbI_3$ inorganic PSCs still face relatively higher open-circuit voltage (V_{OC}) losses (0.5 V) than hybrid perovskites (0.3 V),[9] which is mainly attributed to the substantial charge recombination at the interfaces.[10] Therefore, precise interface engineering for efficient defect passivation and charge transfer plays a crucial role in the preparation of high-performance $CsPbI_3$ PSCs.

Interfacial modification has been proven to be an effective way for reducing the trap state density at the interfaces of perovskite devices, leading to the fabrication of high efficient PSCs. Various materials as electron donors or electron acceptors have been applied to hinder the nonradiative recombination losses in devices by passivating interfacial defects.[11] However, most of them only possess a single passivation effect and cannot improve the comprehensive performance of the device. Therefore, it is of great significance to explore a multifunctional and effective material that is beneficial to charge transfer, defect passivation, and stability improvement.

MXene ($Ti_3C_2T_x$, T: O, OH, and/or F),[12] is a novel 2D carbon-metal composite with some peculiar physical and chemical properties, which has been extensively applied in lithium-ion batteries,[13] sensors,[14] and supercapacitors.[15] Compared with pure carbon-based 2D materials, $Ti_3C_2T_x$ has many functional Ti–X (—OH, F, Cl, Br) bonds, which can not only passivate the defects in PSCs but also improve the charge injection or collection between perovskite and charge transport layer.[16] In addition, $Ti_3C_2T_x$ exhibits good dispersibility in various solvent systems such as ethanol, dimethyl sulfoxide, methanol, dimethylformamide, chlorobenzene, etc.,[17] which ensures that it can be used as an additive or electron-transport/hole-transport materials in PSCs. Recently, Guo et al. introduced MXene into the perovskite active layer to retard the crystallization rate and achieved a PCE of 17.41%.[18] Yang et al. demonstrated that MXene quantum dots (QDs)-modified SnO_2 electron-transport layers (ETLs) could enhance perovskite crystallization.[19] The reported applications of MXene in the perovskite field have mainly focused on the modification of ETLs, and few works have employed MXene

D. Xu, T. Li, Y. Han, X. He, S. Yang, Y. Che, J. Xu, H. Zou, X. Guo, J. Wang, X. Lei, Z. Liu
Key Laboratory of Applied Surface and Colloid Chemistry
Ministry of Education; Shaanxi Key Laboratory for Advanced Energy Devices
Shaanxi Engineering Lab for Advanced Energy Technology
School of Materials Science and Engineering
Shaanxi Normal University
Xi'an 710119, P. R. China
E-mail: xxhe@snnu.edu.cn; zhike2015@snnu.edu.cn

The ORCID identification number(s) for the author(s) of this article can be found under https://doi.org/10.1002/adfm.202203704.

DOI: 10.1002/adfm.202203704

QDs as interfacial materials between perovskites and hole-transport layers (HTLs) to study their effects on hole transport.

In this work, MXene QDs with abundant Ti—F groups were prepared by a liquid-phase exfoliation technology. In order to enhance the stability and efficiency of inorganic $CsPbI_3$ PSCs, fluorine functionalized *p*-type MXene QDs were applied to modify the surface of *n*-type $CsPbI_3$ perovskite. The MXene QDs can not only effectively accelerate charge extraction, but also induce strong interactions with perovskites to passivatate defects and suppress nonradiative recombination. In addition, the abundant fluorine groups in MXene QDs provide an effective barrier against water molecules, which will reduce the degradation of perovskite film. As a result, $CsPbI_3$ PSCs treated with MXene QDs achieve a champion efficiency of 20.44% and a high V_{OC} of 1.22 V. Moreover, the unencapsulated $CsPbI_3$ PSC exhibits an enhanced stability with 93% retention rate of its initial efficiency after aging in air with 25% relative humidity for 600 h.

2. Results and Discussion

$Ti_3C_2F_x$ flakes were prepared by HF-based etching of the Ti_3AlC_2 precursor material. The $Ti_3C_2F_x$ QDs were then obtained from $Ti_3C_2F_x$ flakes by a probe ultrasonic method, as illustrated in **Figure 1**a. The X-ray diffraction (XRD) spectra are illustrated in Figure 1b, showing the patterns of Ti_3AlC_2 bulk, $Ti_3C_2F_x$ flakes, and $Ti_3C_2F_x$ QDs. Ti_3AlC_2 bulk exhibits sharp diffraction peaks, indicating good crystallinity. After removing Al by HF etching, the characteristic diffraction peak (104) of Ti_3AlC_2 disappeared, indicating that the Al layer was successfully removed. The successful synthesis of $Ti_3C_2F_x$ is confirmed by the shift of (002) peak from 9.62° of raw Ti_3AlC_2 to 8.95° of $Ti_3C_2F_x$.[20] When the as-prepared $Ti_3C_2F_x$ was treated by probe ultrasonic process, the (002) peak shifted from 8.95 to 5.85°, proving the transformation of $Ti_3C_2F_x$ flakes into $Ti_3C_2F_x$ QDs.[21] To investigate the surface properties and composition of $Ti_3C_2F_x$ QDs, X-ray photoelectron spectroscopy (XPS) was conducted. As shown in Figure 1c, the XPS spectrum exhibits signals of F 1s, Ti 2p, C 1s, and O 1s.The appearance of strong fluorine peaks clearly indicates the formation of Ti—F groups. Meanwhile, the absence of Al 2p further conforms that the Al layer in raw $Ti_3Al_2C_2$ is completely removed. XRD and XPS results prove that $Ti_3Al_2C_2$ has been tranformed into $Ti_3C_2F_x$ after HF and ultrasonic treatments. The high-resolution Ti 2p peak is shown in Figure 1d. The main Ti 2p peak at about 455.07 eV can be divided into Ti—C, Ti^{2+}, and Ti^{3+},[22] indicating that the Ti_3C_2 structure

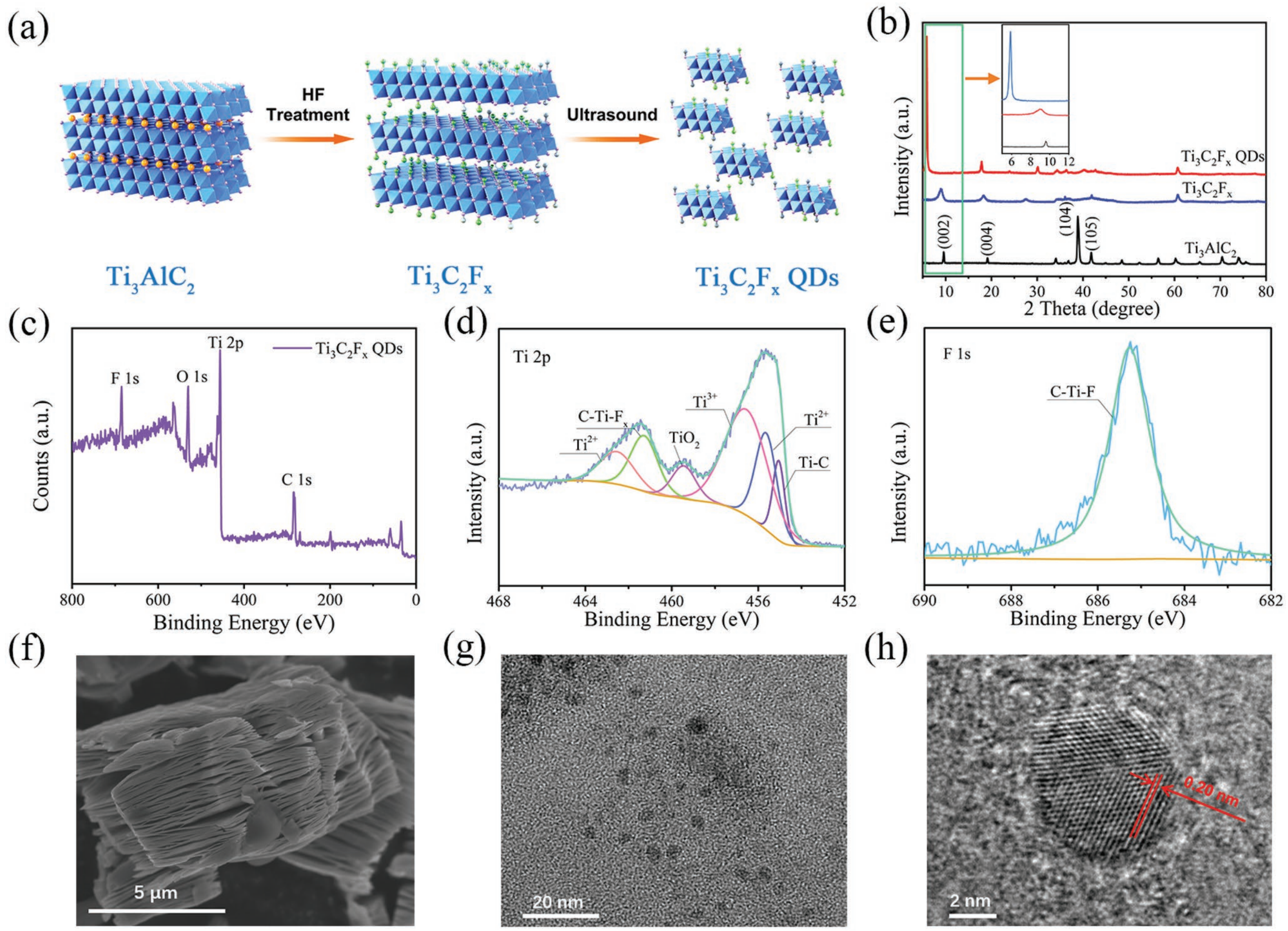

Figure 1. a) Preparation process of $Ti_3C_2F_x$ QDs. b) XRD pattern of Ti_3AlC_2 bulk and $Ti_3C_2F_x$ flake, $Ti_3C_2F_x$ QDs. XPS spectra of c) $Ti_3C_2F_x$ QDs, d) Ti 2p, and e) F 1s. f) SEM image of $Ti_3C_2F_x$ flakes. g) TEM and h) HRTEM images of $Ti_3C_2F_x$ QDs.

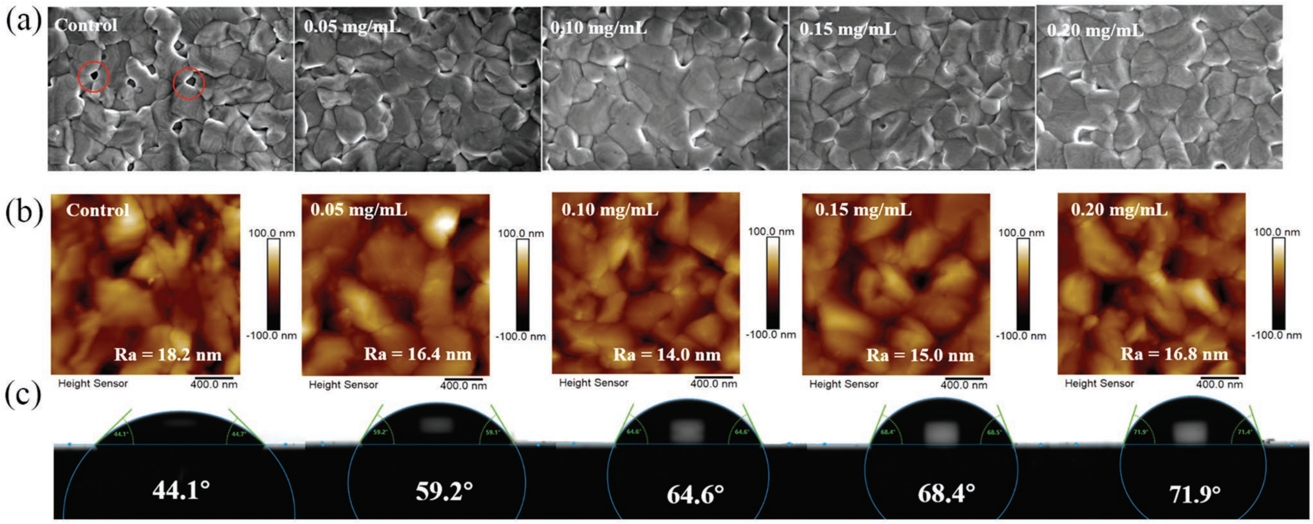

Figure 2. a) Top-view SEM images, b) AFM images, and c) Contact angles of $CsPbI_3$ films with different concentrations of $Ti_3C_2F_x$ QDs treatment.

remains during the etching and ultrasonic process. Figure 1e shows the high-resolution F 1s peak (685.24 eV), which is attributed to C—Ti—F_x,[23] indicating that the $Ti_3C_2T_x$ QDs were successfully terminated by fluorine. The morphologies of Ti_3AlC_2 bulk, $Ti_3C_2F_x$ flakes, and $Ti_3C_2F_x$ QDs were studied by Scanning Electron Microscopy (SEM) and transmission electron microscopy (TEM). After the HF etching process, the Ti_3AlC_2 bulk (Figure S1, Supporting Information) was transformed into few-layer $Ti_3C_2F_x$ flakes (Figure 1f). The $Ti_3C_2F_x$ QDs were then obtained by ultrasonic treatment of $Ti_3C_2F_x$ flakes, and the QDs display uniform size of ≈6 nm (Figure 1g). The high-resolution TEM (HRTEM) image of $Ti_3C_2F_x$ QDs is shown in Figure 1h, clear lattice fringes are observed, indicating the high quality of $Ti_3C_2F_x$ QDs.

The prepared $Ti_3C_2F_x$ QDs with different concentrations were then spin-coated onto $CsPbI_3$ film to study their effects on the crystallinity and absorption of perovskite. As shown in Figure S2a (Supporting Information), the XRD patterns of the control and $Ti_3C_2F_x$ QDs treated $CsPbI_3$ films are similar with two strong characteristic peaks located at 14.51° and 29.05°, corresponding to (110) and (220) crystal planes of α-phase $CsPbI_3$ perovskite, respectively.[24] Clearly, the diffraction and absorption intensities of perovskite films are increased after $Ti_3C_2F_x$ QDs treatment (Figure S2a,b, Supporting Information), indicating that $Ti_3C_2F_x$ QDs treatment favored the crystallinity of $CsPbI_3$ films. All the $CsPbI_3$ films have an identical bandgap of 1.72 eV, which is consistent with the reported bandgap of $CsPbI_3$. SEM was conducted to further study the effect of $Ti_3C_2F_x$ QDs treatment on the perovskite films, as shown in **Figure 2**a. Compared to the control film with many pinholes on the surface, the $Ti_3C_2F_x$ QDs treated films have smoother surface and no pinhole. The average grain size increased from 0.52 µm in the control film to 0.76 µm in the 0.20 mg mL^{-1} $Ti_3C_2F_x$ QDs treated film, and the corresponding grain size distributions are summarized in Figure S3 (Supporting Information). The reduced pinholes and increased grain size are due to secondary grain growth induced by the surface-treatment.[25] The morphologies of perovskite films treated with different concentrations of $Ti_3C_2F_x$ QDs were further studied by atomic force microscopy (AFM). As shown in Figure 2b, the $CsPbI_3$ film with 0.10 mg mL^{-1} $Ti_3C_2F_x$ QDs treatment exhibits the smoothest surface compared with other perovskite films, which means that spin-coating of $Ti_3C_2F_x$ QDs with appropriate concentration helps to reduce the surface roughness of perovskite. In order to investigate the effect of $Ti_3C_2F_x$ QDs on the humidity tolerance of the perovskite films, water contact angle measurements were carried out (Figure 2c). The contact angle of the perovskite films increases with the increasing concentration of $Ti_3C_2F_x$ QDs, which is attributed to the increase of fluorine atoms on the perovskite film, proving that the $Ti_3C_2F_x$ QDs can improve the humidity tolerance of $CsPbI_3$ films and mitigate their degradation in air.[26]

The effect of $Ti_3C_2F_x$ QDs treatment on the electronic states of perovskite was studied by XPS spectroscopy (**Figure 3**). The XPS spectrum of the $CsPbI_3$ film with $Ti_3C_2F_x$ QDs shows a peak at 683.5 eV, corresponding to F 1s (Figure 3a), which demonstrates the presence of $Ti_3C_2F_x$ QDs on the perovskite film. Figure 3b–d shows the XPS spectra of the Pb 4f, I 3d, and Cs 3d peaks. Notably, the Cs 3d peaks shift slightly, while the Pb 4f and I 3d peaks obviously shift to lower binding energies after $Ti_3C_2F_x$ QDs treatment, indicating the strong interaction between the $Ti_3C_2F_x$ QDs and Pb/I in the perovskite film.[27] In addition, it suggests that the perovskite surface can be electrostatically passivated by $Ti_3C_2F_x$ QDs. The strong interaction between $Ti_3C_2F_x$ QDs and PbI_2 was further confirmed by the XPS measurement. As shown in Figure 3e,f, the Pb 4f and F 1s peaks exhibit an appreciable shift, while the Ti 2p peaks are almost unchanged (Figure S4, Supporting Information). All XPS results indicate that the strong Pb—F bonds can be formed between $Ti_3C_2F_x$ QDs and $CsPbI_3$, which is conductive to the Pb-related defects passivation and the stability of perovskite.[26a,b]

The steady-state photoluminescence (PL) and time-resolved photoluminescence (TRPL) decay measurements were conducted to study the charge recombination in perovskite films. As shown in **Figure 4**a, the perovskite with $Ti_3C_2F_x$ QDs

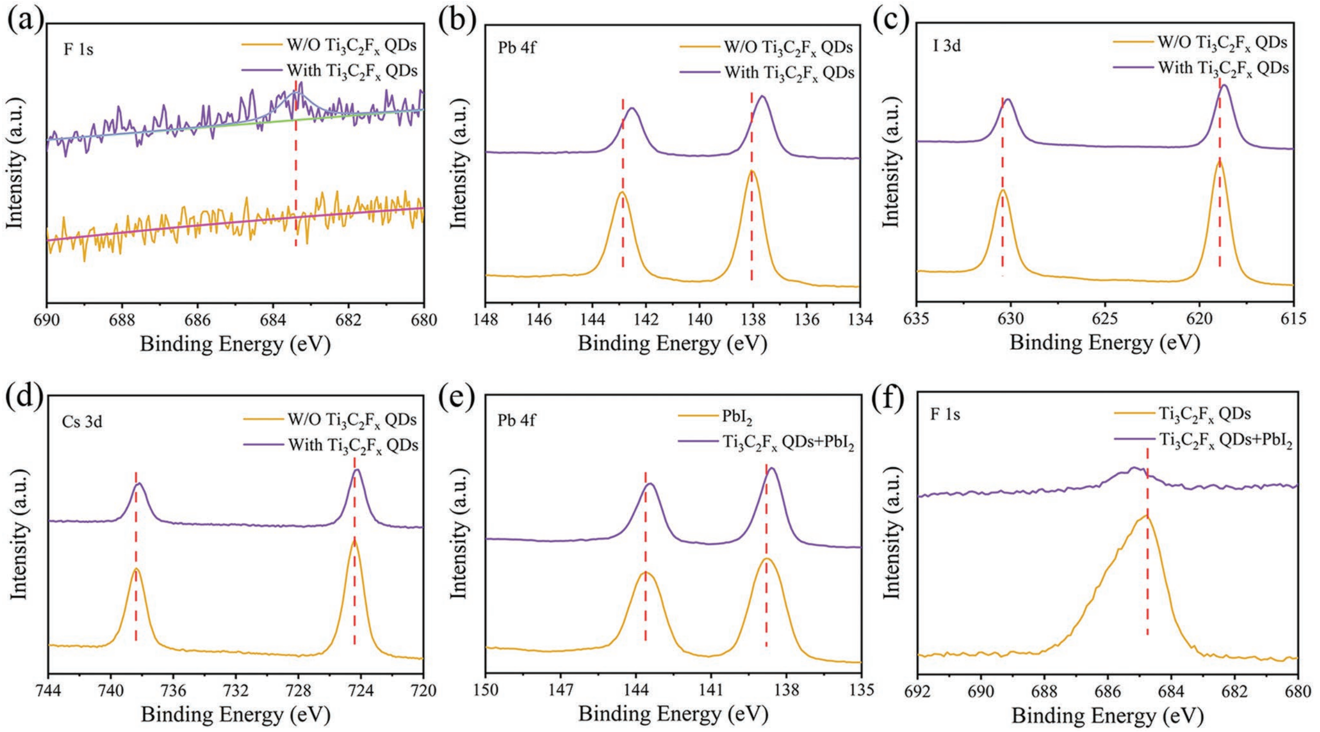

Figure 3. XPS spectra of a) F 1s, b) Pb 4f, c) I 3d, and d) Cs 3d of the $CsPbI_3$ films with or without $Ti_3C_2F_x$ QDs treatment. XPS spectra of e) Pb 4f and f) F 1s of $Ti_3C_2F_x$ QDs with or without PbI_2 additive.

treatment exhibits an enhanced PL emission compared with the control film, confirming the suppression of nonradiative recombination by coating $Ti_3C_2F_x$ QDs. The enhanced PL intensity can be ascribed to the passivation effect of $Ti_3C_2F_x$ QDs on the defects of perovskite surface.[28] Figure 4b shows the TRPL decay curves, which fits well by using a biexponential

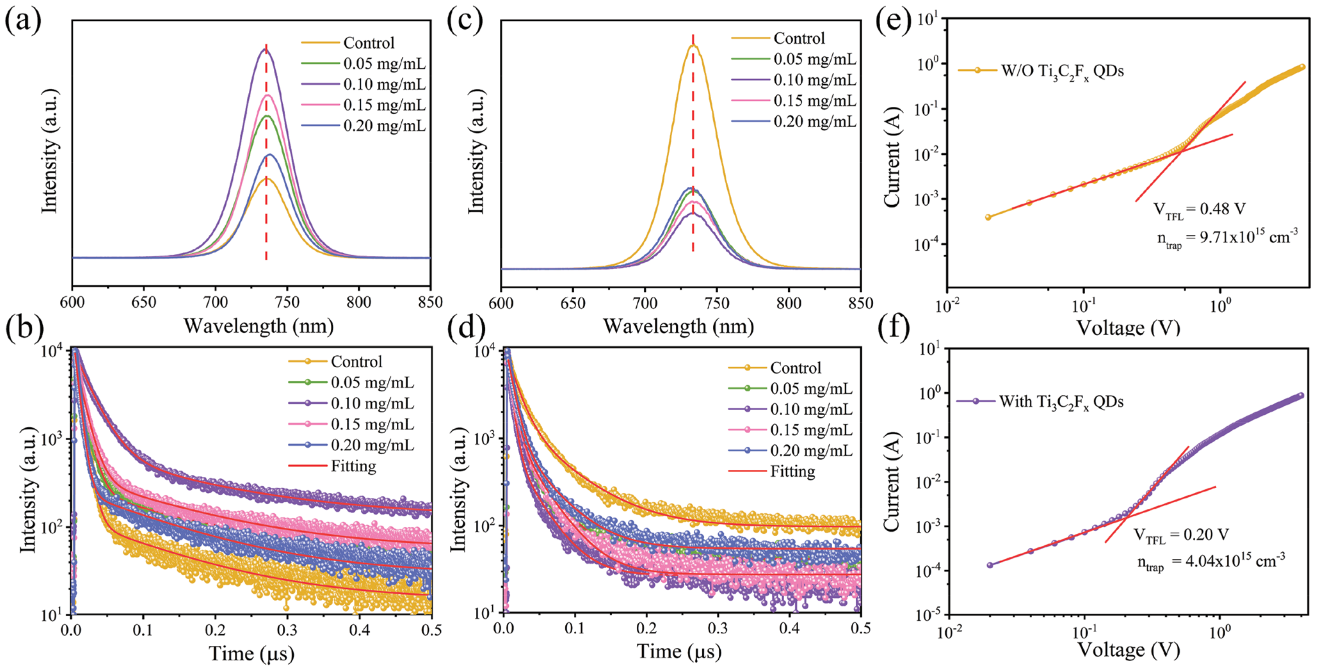

Figure 4. a) PL and b) TRPL spectra of $CsPbI_3$ films with different concentrations of $Ti_3C_2F_x$ QDs treatment. c) PL and d) TRPL spectra of $CsPbI_3$/Spiro with different concentrations of $Ti_3C_2F_x$ treatment. The space-charge-limited current versus voltage for e) the FTO/TiO_2/$CsPbI_3$/PCBM/Ag and f) FTO/TiO_2/$CsPbI_3$/$Ti_3C_2F_x$ QDs /PCBM/Ag device.

function: $f(t) = A_1\exp(-t/\tau_1) + A_2\exp(-t/\tau_2)$, where A_1 and A_2 are the decay amplitudes, and τ is the decay time constant.[29] The fitted parameters are summarized in Table S1 (Supporting Information). The average carrier lifetime of the control $CsPbI_3$ film is significantly improved from 38.84 to 69.93 ns after $Ti_3C_2F_x$ QDs treatment, suggesting lower charge recombination in the $Ti_3C_2F_x$ QDs-treated perovskite films. The enhanced PL intensity and increased average carrier lifetime prove that $Ti_3C_2F_x$ QDs can effectively inhibit nonradiative recombination and prolong the carrier lifetime of the $CsPbI_3$ film.[3e]

To assess the influence of $Ti_3C_2F_x$ QDs on the charge transfer dynamics at the perovskite/Spiro-OMeTAD interface, PL, and TRPL measurements are conducted on the devices with a structure of perovskite ($Ti_3C_2F_x$ QDs)/Spiro-OMeTAD. As shown in Figure 4c, compared to the control sample, the PL intensity of the device with $Ti_3C_2F_x$ QDs treatment displays obvious quenching, implying a more efficient hole extraction process between perovskite and Spiro-OMeTAD. Figure 4d shows the TRPL results and the corresponding fitted parameters are listed in Table S2 (Supporting Information). In the biexponential function corresponding to the perovskite ($Ti_3C_2F_x$ QDs)/Spiro-OMeTAD structure, τ_1 is related to PL quenching originating from charge transfer at the perovskite/Spiro-OMeTAD interface, while τ_2 is related to the radiative recombination of trapped charges within the perovskite layer.[26b] Clearly, τ_1 is significantly reduced when the $Ti_3C_2F_x$ QDs were introduced into the perovskite/Spiro-OMeTAD interface. The average carrier lifetime of $Ti_3C_2F_x$ QDs treated device is about 13.94 ns, which is much shorter than that of the control sample (34.97 ns). The PL and TRPL results suggest that the separation and transmission of photogenerated charge between perovskite and Spiro-OMeTAD is promoted by $Ti_3C_2F_x$ QDs treatment. The conclusion is supported by measurement of hole transport properties. As shown in Figure S5 (Supporting Information), Hall effect measurement shows that the prepared $Ti_3C_2F_x$ QDs are *p*-type semiconductors, which means that the $Ti_3C_2F_x$ QDs are beneficial to hole extraction and transport. Furthermore, space-charge-limited-current (SCLC) measurement was applied to further investigate the influence of $Ti_3C_2F_x$ QDs on the hole-transport. The hole-only devices with fluorine-doped tin oxide (FTO)/PEDOT:PSS/Spiro-OMeTAD/Au or FTO/PEDOT:PSS/$Ti_3C_2F_x$ QDs/Spiro-OMeTAD/Au structure were prepared (Figure S6, Supporting Information). The current-voltage (*J*–*V*) curves at high voltage are fitted by $J_{(V)} = (9/8)\varepsilon\varepsilon_0\mu V^2/d^3$, where ε is the dielectric constant and d is the film thickness of Spiro-OMeTAD.[30] The hole mobility of Spiro-OMeTAD without $Ti_3C_2F_x$ QDs is 1.59×10^{-4} cm^2 V^{-1} S^{-1}, which increases to 3.50×10^{-4} cm^2 V^{-1} S^{-1} after $Ti_3C_2F_x$ QDs treatment. Therefore, $Ti_3C_2F_x$ QDs treatment can not only improve the electrical properties of perovskite, but also enhance the mobility and hole extraction ability of Spiro-OMeTAD.

The space-charge limited current method was also applied to quantitatively evaluate the electron trap-state density (n_{trap}) in the $CsPbI_3$ films by using a device structure of FTO/TiO_2/perovskite/PCBM/Ag. The n_{trap} values are calculated using the equation: $n_{trap} = 2\varepsilon_0\varepsilon V_{TFL}/eL^2$, where ε_0 is the vacuum permittivity, ε is the relative dielectric constant of the perovskite, e is the electron charge, V_{TFL} is the trap-filled limit voltage, and L is the thickness of the perovskite film.[10b,31] Figure 4e,f show the dark *J*–*V* characteristics of the control and $Ti_3C_2F_x$ QDs treated devices. The obtained n_{trap} values are 9.71×10^{15} and 4.04×10^{15} cm^{-3} for control and $Ti_3C_2F_x$ QDs treated devices, respectively. The defect density decreased by more than half after $Ti_3C_2F_x$ QDs treatment, which can be attributed to the passivation effect of $Ti_3C_2F_x$ QDs.[26a,32]

The $CsPbI_3$ PSCs with FTO/TiO_2/$CsPbI_3$($Ti_3C_2F_x$ QDs)/Spiro-OMeTAD/Au structure were fabricated to evaluate the effect of $Ti_3C_2F_x$ QDs on the photovoltaic performance, as shown in **Figure 5**a. Ultraviolet photoelectron spectroscopy (UPS) was conducted to determine the surface band structure of perovskite films with and without $Ti_3C_2F_x$ QDs treatment (Figure S7, Supporting Information). The valance band (VB) is 5.54 eV for the control film and 5.43 eV for $Ti_3C_2F_x$ QDs treated film, respectively, the detailed data is shown in Table S3 (Supporting Information). The corresponding energy levels of $CsPbI_3$ PSCs are shown in Figure 5b, wherein the band structures of TiO_2 and Spiro-OMeTAD and work functions of FTO, Au electrodes are also illustrated.[33] The energy difference between the valence bands of the $CsPbI_3$ film and Spiro-OMeTAD is remarkably reduced after $Ti_3C_2F_x$ QDs treatment, which is conductive to hole transport and consistent with the PL and TRPL results.

Figure 5c displays the *J*–*V* curves of control and $Ti_3C_2F_x$ QDs treated PSCs. The control PSC shows a champion PCE of 18.39% with a V_{OC} of 1.15 V, a short circuit current (J_{SC}) of 20.02 mA cm^{-2}, and a fill factor (FF) of 79.68%. In contrast, the $Ti_3C_2F_x$ QDs-treated device exhibits higher PCE of 20.44%, with a V_{OC} of 1.22 V, a J_{SC} of 20.59 mA cm^{-2}, and a FF of 81.55%. The enhanced performance for the $Ti_3C_2F_x$ QDs treated device can be ascribed to the excellent passivation effect of $Ti_3C_2F_x$ QDs and promoted charge transfer between perovskite and Spiro-OMeTAD. The E_{loss} of the optimized device is reduced to as low as 0.5 eV, which is one of the minimum values for the reported $CsPbX_3$ PSCs. As shown in Figure 5d, the external quantum efficiency (EQE) spectra were performed to verify the J_{SC} values obtained from *J*–*V* curves. The integrated J_{SC} values are 20.02 and 20.43 mA cm^{-2} for the control and $Ti_3C_2F_x$ QDs treated devices, respectively, which match well with the *J*–*V* results. Figure 5e shows the steady power output (SPO) of the $CsPbI_3$ PSCs tracking at maximum power. The $Ti_3C_2F_x$ QDs treated PSC exhibits a stabilized PCE of 20.40% for a testing period of 1200 s, which is much higher than that of the control device (18.40%). The statistical photovoltaic parameters of 40 individual control and optimized devices are presented in Figure S8 (Supporting Information). Compared with the control devices, the $Ti_3C_2F_x$ QDs treated devices show higher average PCE (19.55% vs 18.10%) and excellent reproducibility.

To elucidate the reason for the improved V_{OC}, the built-in-potential (V_{bi}) of PSCs was measured by recording the capacitance–voltage (*C*–*V*) curves under dark conditions. According to the Mott–Schottky equation: $C^{-2} = (2(V_{bi}-V))/(A^2e\varepsilon\varepsilon_0N_A)$, the V_{bi} for optimized PSC is 1.15 V, which is higher than that of the control device (1.04 V). The higher V_{bi} can provide an enhanced driving force for charge separation and lead to higher V_{OC} (Figure 5f).[34] The V_{OC} was measured under various light intensities to evaluate defect-assisted recombination of PSCs. As shown in Figure 5g, the slope of the curve decreases drastically from 1.77 to 1.17 kT q^{-1} after $Ti_3C_2F_x$ QDs treatment, indicating

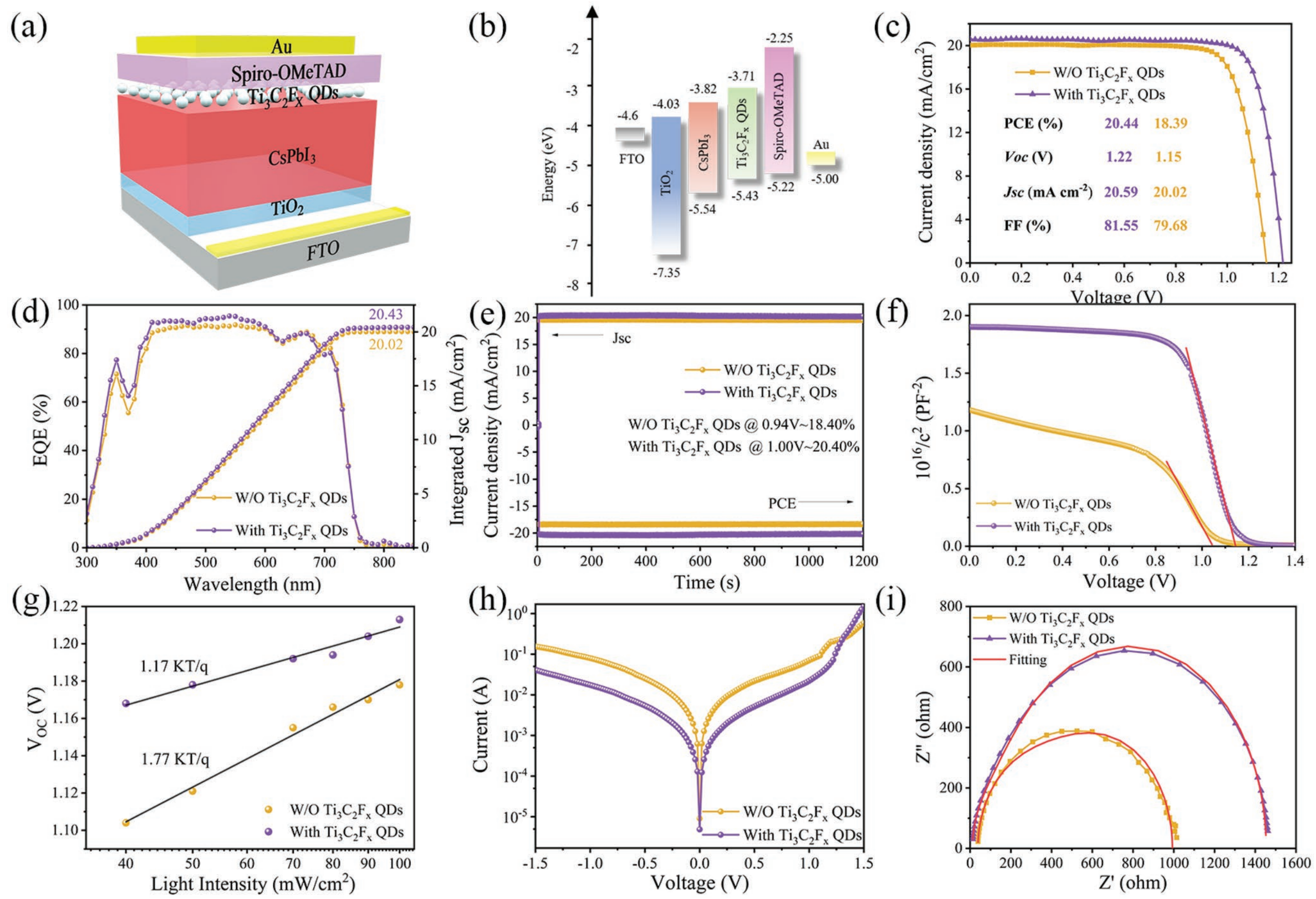

Figure 5. a) Schematic image of a $CsPbI_3$ PSC with the structure FTO/TiO_2/$CsPbI_3$/$Ti_3C_2F_x$/Spiro-OMeTAD/Au, b) Schematic energy-level alignment of the $CsPbI_3$ PSC with $Ti_3C_2F_x$ treatment, c) *J–V* curves, d) EQE spectra, e) stable output curves, f) *C–V*, g) open-circuit voltage dependence on light intensity, h) *J–V* curves under dark conditions, and i) Nyquist plots of the $CsPbI_3$ PSC with $Ti_3C_2F_x$ treatment.

that the defect-assisted recombination is suppressed.[35] Further, the dark *J–V* curves of PSCs were measured to evaluate the charge transport properties of the devices in Figure 5h. It is obvious that the $Ti_3C_2F_x$ QDs treated PSC possesses smaller leakage current than that of the control device, suggesting a decreased carrier generation rate and background carrier density in the device.[36] The dark *J–V* result also confirms that the trap density in the device is reduced by $Ti_3C_2F_x$ QDs passivation. In addition, the electrochemical impedance spectroscopy (EIS) measurements were conducted to further investigate the charge transfer and recombination process in $CsPbI_3$ PSCs, and the corresponding Nyquist plots are shown in Figure 5i, the equivalent circuit model and the fitting parameters are listed in Figure S9 and Table S4 (Supporting Information), respectively. In comparison with the control device, the $Ti_3C_2F_x$ QDs treated device presents smaller R_s/R_{tr} and higher R_{rec}, indicating that $Ti_3C_2F_x$ QDs can effectively suppress the charge carrier recombination and boost charge transfer in $CsPbI_3$ PSCs. Therefore, the $Ti_3C_2F_x$ QDs treatment can passivate the trap states and improve the charge transfer, consequently resulting in high photovoltaic performance.

To study the effect of $Ti_3C_2F_x$ QDs treatment on the stability of $CsPbI_3$ PSCs, the long-term stabilities of unencapsulated $CsPbI_3$ films and PSCs were measured. **Figure 6**a shows photographs of $CsPbI_3$ films stored for 120 h in air with a relative humidity (RH) of 35%. It is obvious that the air stability of $Ti_3C_2F_x$ QDs treated film is significantly improved. The result is also supported by XRD measurement. As shown in Figure 6b, all the pristine $CsPbI_3$ films are α-phase with cubic crystal structure. After storage in air for 120 h, the XRD peak intensity of the control film decreased significantly with new peaks appearing at 10.15° and 31.50°, corresponding to the δ-phase $CsPbI_3$. In contrast, no change has observed in the XRD spectrum for $Ti_3C_2F_x$ QDs treated $CsPbI_3$ film after 120 h, indicating that the α-phase crystalline structure of $CsPbI_3$ is preserved. Figure 6c shows the storage stability of unencapsulated $CsPbI_3$ PSCs in air with a relative humidity of ≈35%. Obviously, the $Ti_3C_2F_x$ QDs treated device exhibits better stability, maintaining ≈93% of its initial efficiency after 600 h storage, whereas the PCE of the control device decreases dramatically to ≈72% of its initial value during the same period. These results indicate that the stability of PSCs can be effectively improved by $Ti_3C_2F_x$ QDs treatment.

3. Conclusion

In summary, the $Ti_3C_2F_x$ QDs were successfully prepared and introduced onto the top of the perovskite film as passivation

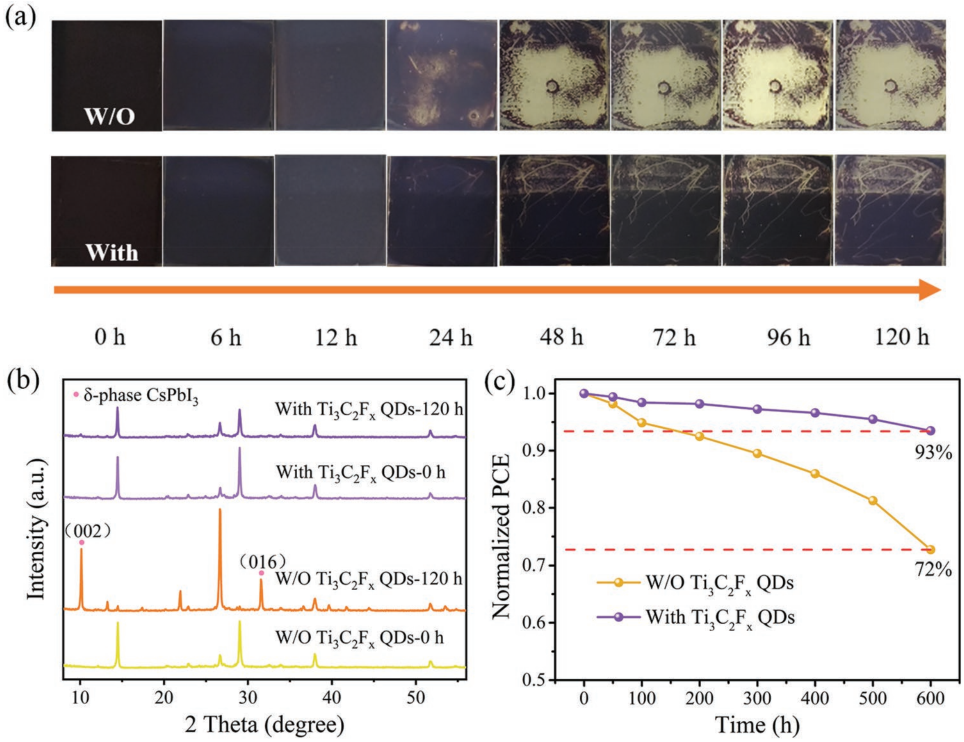

Figure 6. a) Photographs of control and $Ti_3C_2F_x$ QDs-treated $CsPbI_3$ films aged in ambient air conditions (RH: ≈35%, T = 25 °C). b) XRD patterns of perovskite films without and with $Ti_3C_2F_x$ QDs treatment at 35% RH for 0 and 120 h. c) Air stability of the $CsPbI_3$ PSCs without and with $Ti_3C_2F_x$ QDs treatment.

materials. It is found that $Ti_3C_2F_x$ QDs can not only provide efficient pathways for hole transfer but also passivate defects to reduce nonradiative charge recombination on the surface of perovskite films. Based on the $Ti_3C_2F_x$ QDs treatment, strong interactions can be formed between perovskite and fluorine ions of $Ti_3C_2F_x$ QDs, resulting in lower trap state density and longer carrier lifetime for the perovskite films. Meanwhile, a well-matched energy level alignment between Spiro-OMeTAD and $CsPbI_3$ is constructed by $Ti_3C_2F_x$ QDs treatment. In addition, the $Ti_3C_2F_x$ QDs provide effective barrier against water molecules, hindering the degradation of perovskite film. As a result, the champion $CsPbI_3$ PSCs with $Ti_3C_2F_x$ QDs treatment achieved a high PCE of 20.44% with a V_{OC} of 1.22 V and high air stability. This work taps the potential of $Ti_3C_2F_x$ QDs as effective passivation materials to fabricate high-performance inorganic PSCs.

4. Experimental Section

Materials: Hydrogen lead triiodide ($HPbI_3$), Cesium iodide (CsI), and Spiro-OMeTAD were purchased from Xi'an Polymer Light Technology Corp. Titanium aluminum carbon (Ti_3AlC_2) was purchased from Beijing fosman Technology Co. Ltd. 40% Hydrofluoric acid (HF) was purchased from Sinopharm Group Chemical Reagent Co. Ltd. N,N-dimethylformamide (DMF) and dimethyl sulfoxide (DMSO) were purchased from Shanghai Aladdin Biochemical Technology Co. Ltd. 4-tert-butylpyridine (*t*-BP), chlorobenzene (CB), and lithium bis(trifluoromethylsulfonyl)imide salt (Li-TFSI) were purchased from Sigma–Aldrich. 25% tetramethylammonium hydroxide (TMAOH) was purchased from Sigma–Aldrich.

Synthesis of $Ti_3C_2F_x$ QDs: HF as etchant: One gram of Ti_3AlC_2 powder was slowly added to a plastic beaker containing 20 mL of 40% HF, and the resulting suspension was stirred at room temperature for 3 days so that HF and Ti_3AlC_2 could fully react under vigorous stirring.[37] The etched samples were then suction filtered, washed with deionized water, and freeze-dried to obtain layered $Ti_3C_2F_x$ powder. The lyophilized $Ti_3C_2F_x$ powder was added to a 25% TMAOH aqueous solution followed by N_2 to protect the $Ti_3C_2F_x$ from oxidation. After standing at room temperature for additional 12 h, the mixture was shaken overnight and the resulting suspension was centrifuged at 3500 rpm for 30 min to remove unstripped multilayer $Ti_3C_2F_x$. It was then centrifuged at 15 000 rpm for 10 min to obtain $Ti_3C_2F_x$ monolayer (dark green supernatant), and the supernatant was collected for the next experiment.

Preparation of $Ti_3C_2F_x$ QDs: Probe ultrasonic method uses a tip sonicator to sonicate the exfoliated $Ti_3C_2F_x$ nanosheet suspension; $Ti_3C_2F_x$ QDs solution was obtained after sonicating for 30 min at a power of 600 W. The produced $Ti_3C_2F_x$ QDs solution was freeze-dried to obtain $Ti_3C_2F_x$ QDs powder, and 10 mg of the powder was weighed and added to 10 mL of chlorobenzene solution to prepare 1 mg mL^{-1} $Ti_3C_2F_x$ QDs dispersion. In order to uniformly disperse $Ti_3C_2F_x$ QDs in chlorobenzene solution, the solution was sonicated for 30 min and diluted to 0.05, 0.10, 0.15, and 0.20 mg mL^{-1}, respectively.

Device Fabrication: FTO was cleaned with special cleaning concentrate of cuvettes and dried with an air gun. The TiO_2 layer was deposited by immersing FTO glass substrates in 200 mL aqueous solution containing 4.5 mL titanium tetrachloride at 70 °C for 60 min, then rinsed with distilled water and annealed at 200 °C for 30 min. Perovskite solution (0.745 м) was prepared by using $HPbI_3$ and CsI (1:1) as precursors, DMSO and DMF (v:v = 1:9) as solvent, which was stirred for 12 h. The perovskite precursor solution was spin-coated on the UV-Ozone-treated TiO_2/FTO glass in a process of 1000 rpm for 10 s, 3000 rpm for 30 s in a N_2 filled glove box. The perovskite precursor film was annealed at 170 °C for 50 min to crystallize.

$Ti_3C_2F_x$ QDs solutions with different concentrations were spin-coated at 3000 rpm for 40 s to modify the surface of perovskite, and then annealed at 100 °C for 5 min. Spiro-OMeTAD solution (90 mg mL^{-1}) with 36 µL *t*-BP and 22 µL Li-TFSI (520 mg mL^{-1}) solution in acetonitrile was coated onto perovskite film at 5000 rpm for 30 s as hole transport layer. Finally, an 80-nm Au electrode was deposited by thermal evaporation through a shadow mask to form a device with an active area of 0.09 cm^2.

Device Characterization: XRD patterns were collected from a D/Max-3c diffractometer (DX-2700) with Cu Kα. XPS was carried out using ESCALAB250Xi, Thermo Fisher Scientific. The SEM images were obtained by field-emission scanning electron microscopy (SEM, HITACHI, SU-8020). The TEM images were conducted by JEOL-JEM 2800. UPS was measured by ESCALAB250Xi, Thermo Fisher Scientific. Contact angle measurements were performed on measuring optical contact angle tester (Kruss, Germany). AFM images were taken by BRUKER Atomsa Force Microscope. The PL spectra and TRPL spectra were measured by using Edinburgh Instruments Ltd. FLS980 spectrometer with excitation wavelength 510 nm. The *J–V* curves were obtained using a Keitheley 2400 source under simulated sunlight (AM 1.5G, SAN-EIELECTRIC XES-40S2-CE). EQE tests were measured by a QTest Station 2000ADI (Crowntech, Inc. USA), calibrated prior to testing with a standard silicon detector over a wavelength range of 500 to 850 nm. EIS and *C–V* results obtained using Solartron electrochemical workstation. The absorption spectra were measured using a UV–vis NIR spectrophotometer (PerkinElmer, Lambda 950). The Hall effect was obtained using a semiconductor alternating current test system (van der Pauw low temperature Hall).

Statistics Analysis: All statistics analysis were performed with Origin 2018. All the data keep two significant digits after the decimal points by the rounding-off method. The data obtained from SEM, TEM, AFM, UV–vis, PL, TRPL, Contact angles, XPS, UPS, *J–V*, and EQE are the original data without normalized. The other data were obtained by transferring corresponding original data according to the calculation formula. Linear fittings were applied to Mott–Gurney plot (Figure 4e,f and Figure S6 Supporting Information), *V*oc versus light intensity plots (Figure 5g) and Mott–Schottky plots (Figure 5f). Bi-exponential decay function was applied to TRPL decays to infer the carrier extraction/recombination dynamics. The statistical distribution data of PCE, *J*sc, *V*oc and FF were got from 40 devices each.

Supporting Information

Supporting Information is available from the Wiley Online Library or from the author.

Acknowledgements

D.X. and T.L. contributed equally to this work. The authors acknowledge support from the National Natural Science Foundation of China (62074095), National Natural Science Foundation of China (51702203) and the Natural Science Basic Research Plan in Shaanxi Province of China (2020JQ-408), the Shaanxi Sanqin Scholars Innovation Team, the Fundamental Research Funds for the Central Universities (GK202002001).

Conflict of Interest

The authors declare no conflict of interest.

Data Availability Statement

Research data are not shared.

Keywords

high efficiency, high voltages, inorganic perovskites, MXenes, $Ti_3C_2F_x$ QDs

Received: April 1, 2022
Revised: May 2, 2022
Published online:

[1] National Renewable Energy Laboratory (NREL), Best Cell Efficiencies, https://www.nrel.gov/pv/cell-efficiency.html, **2022**.
[2] a) F. Lang, O. Shargaieva, V. V. Brus, H. C. Neitzert, J. Rappich, N. H. Nickel, *Adv. Mater.* **2018**, *30*, 1702905; b) R. Wang, M. Mujahid, Y. Duan, Z. K. Wang, J. Xue, Y. Yang, *Adv. Funct. Mater.* **2019**, *29*, 1808843; c) E. J. Juarez-Perez, L. K. Ono, M. Maeda, Y. Jiang, Z. Hawash, Y. Qi, *J. Mater. Chem. A* **2018**, *6*, 9604.
[3] a) I. Chung, J. H. Song, J. Im, J. Androulakis, C. D. Malliakas, H. Li, A. J. Freeman, J. T. Kenney, M. G. Kanatzidis, *J. Am. Chem. Soc.* **2012**, *134*, 8579; b) W. Xiang, W. Tress, *Adv. Mater.* **2019**, *31*, 1902851; c) A. Ho-Baillie, M. Zhang, C. F. J. Lau, F.-J. Ma, S. Huang, *Joule* **2019**, *3*, 938; d) J. Liang, C. Wang, Y. Wang, Z. Xu, Z. Lu, Y. Ma, H. Zhu, Y. Hu, C. Xiao, X. Yi, G. Zhu, H. Lv, L. Ma, T. Chen, Z. Tie, Z. Jin, J. Liu, *J. Am. Chem. Soc.* **2016**, *138*, 15829; e) Y. Han, H. Zhao, C. Duan, S. Yang, Z. Yang, Z. Liu, S. Liu, *Adv. Funct. Mater.* **2020**, *30*, 1909972; f) M. Kulbak, D. Cahen, G. Hodes, *J. Phys. Chem. Lett.* **2015**, *6*, 2452.
[4] a) G. E. Eperon, G. M. Paternò, R. J. Sutton, A. Zampetti, A. A. Haghighirad, F. Cacialli, H. J. Snaith, *J. Mater. Chem. A* **2015**, *3*, 19688; b) Y. Wang, M. I. Dar, L. K. Ono, T. Zhang, M. Kan, Y. Li, L. Zhang, X. Wang, Y. Yang, X. Gao, Y. Qi, M. Gratzel, Y. Zhao, *Science* **2019**, *365*, 591; c) P. Wang, X. Zhang, Y. Zhou, Q. Jiang, Q. Ye, Z. Chu, X. Li, X. Yang, Z. Yin, J. You, *Nat. Commun.* **2018**, *9*, 2225.
[5] a) S. Xiang, Z. Fu, W. Li, Y. Wei, J. Liu, H. Liu, L. Zhu, R. Zhang, H. Chen, *ACS Energy Lett.* **2018**, *3*, 1824; b) P. Luo, W. Xia, S. Zhou, L. Sun, J. Cheng, C. Xu, Y. Lu, *J. Phys. Chem. Lett.* **2016**, *7*, 3603.
[6] a) W. Xiang, Z. Wang, D. J. Kubicki, X. Wang, W. Tress, J. Luo, J. Zhang, A. Hofstetter, L. Zhang, L. Emsley, M. Gratzel, A. Hagfeldt, *Nat. Commun.* **2019**, *10*, 4686; b) S. Tan, J. Shi, B. Yu, W. Zhao, Y. Li, Y. Li, H. Wu, Y. Luo, D. Li, Q. Meng, *Adv. Funct. Mater.* **2021**, *31*, 2010813.
[7] a) X. Gu, W. Xiang, Q. Tian, S. Liu, *Angew. Chem.* **2021**, *133*, 23348; b) J. Yuan, X. Ling, D. Yang, F. Li, S. Zhou, J. Shi, Y. Qian, J. Hu, Y. Sun, Y. Yang, X. Gao, S. Duhm, Q. Zhang, W. Ma, *Joule* **2018**, *2*, 2450.
[8] S. M. Yoon, H. Min, J. B. Kim, G. Kim, K. S. Lee, S. I. Seok, *Joule* **2021**, *5*, 183.
[9] M. Jeong, I. W. Choi, E. M. Go, Y. Cho, M. Kim, B. Lee, S. Jeong, Y. Jo, H. W. Choi, J. Lee, J. H. Bae, S. K. Kwak, D. S. Kim, C. Yang, *Science* **2020**, *369*, 1615.
[10] a) Z. Guo, A. K. Jena, I. Takei, G. M. Kim, M. A. Kamarudin, Y. Sanehira, A. Ishii, Y. Numata, S. Hayase, T. Miyasaka, *J. Phys. Chem. Lett.* **2020**, *142*, 9725; b) H. Zhao, Y. Han, Z. Xu, C. Duan, S. Yang, S. Yuan, Z. Yang, Z. Liu, S. Liu, *Adv. Energy Mater.* **2019**, *9*, 1902279; c) Q. Ye, Y. Zhao, S. Mu, F. Ma, F. Gao, Z. Chu, Z. Yin, P. Gao, X. Zhang, J. You, *Adv. Mater.* **2019**, *31*, 1905143.
[11] a) B. Yang, J. Suo, E. Mosconi, D. Ricciarelli, W. Tress, F. De Angelis, H.-S. Kim, A. Hagfeldt, *ACS Energy Lett.* **2020**, *5*, 3159; b) Y. Wang, T. Zhang, M. Kan, Y. Zhao, *J. Am. Chem. Soc.* **2018**, *140*, 12345; c) B. Li, Y. Zhang, L. Fu, T. Yu, S. Zhou, L. Zhang, L. Yin, *Nat. Commun.* **2018**, *9*, 1076; d) X. Gu, W. Xiang, Q. Tian, S. F. Liu, *Angew. Chem.* **2021**, *60*, 23164.
[12] a) M. Naguib, M. Kurtoglu, V. Presser, J. Lu, J. Niu, M. Heon, L. Hultman, Y. Gogotsi, M. W. Barsoum, *Adv. Mater.* **2011**, *23*, 4207; b) A. D. Dillon, M. J. Ghidiu, A. L. Krick, J. Griggs, S. J. May,

Y. Gogotsi, M. W. Barsoum, A. T. Fafarman, *Adv. Funct. Mater.* **2016**, *26*, 4162; c) M. Alhabeb, K. Maleski, B. Anasori, P. Lelyukh, L. Clark, S. Sin, Y. Gogotsi, *Chem. Mater.* **2017**, *29*, 7633.
[13] a) Q. Zhao, Q. Zhu, J. Miao, P. Zhang, P. Wan, L. He, B. Xu, *Small* **2019**, *15*, e1904293; b) X. Liang, A. Garsuch, L. F. Nazar, *Angew. Chem.* **2015**, *127*, 3979.
[14] D. H. Ho, Y. Y. Choi, S. B. Jo, J. M. Myoung, J. H. Cho, *Adv. Mater.* **2021**, *33*, 2005846.
[15] a) Z. Zhao, S. Wang, F. Wan, Z. Tie, Z. Niu, *Adv. Funct. Mater.* **2021**, *31*, 2101302; b) C. J. Zhang, L. McKeon, M. P. Kremer, S. H. Park, O. Ronan, A. Seral-Ascaso, S. Barwich, C. O. Coileain, N. McEvoy, H. C. Nerl, B. Anasori, J. N. Coleman, Y. Gogotsi, V. Nicolosi, *Nat. Commun.* **2019**, *10*, 1795.
[16] a) X. Chen, W. Xu, N. Ding, Y. Ji, G. Pan, J. Zhu, D. Zhou, Y. Wu, C. Chen, H. Song, *Adv. Funct. Mater.* **2020**, *30*, 2003295; b) Q. Peng, J. Guo, Q. Zhang, J. Xiang, B. Liu, A. Zhou, R. Liu, Y. Tian, *J. Am. Chem. Soc.* **2014**, *136*, 4113; c) J. Luo, X. Tao, J. Zhang, Y. Xia, H. Huang, L. Zhang, Y. Gan, C. Liang, W. Zhang, *ACS Nano* **2016**, *10*, 2491.
[17] K. Maleski, V. N. Mochalin, Y. Gogotsi, *Chem. Mater.* **2017**, *29*, 1632.
[18] Z. Guo, L. Gao, Z. Xu, S. Teo, C. Zhang, Y. Kamata, S. Hayase, T. Ma, *Small* **2018**, *14*, 1802738.
[19] Y. Yang, H. Lu, S. Feng, L. Yang, H. Dong, J. Wang, C. Tian, L. Li, H. Lu, J. Jeong, S. M. Zakeeruddin, Y. Liu, M. Grätzel, A. Hagfeldt, *Energy Environ. Sci.* **2021**, *14*, 3447.
[20] a) T. Chen, G. Tong, E. Xu, H. Li, P. Li, Z. Zhu, J. Tang, Y. Qi, Y. Jiang, *J. Mater. Chem. A* **2019**, *7*, 20597; b) Y. Wang, P. Xiang, A. Ren, H. Lai, Z. Zhang, Z. Xuan, Z. Wan, J. Zhang, X. Hao, L. Wu, M. Sugiyama, U. Schwingenschlogl, C. Liu, Z. Tang, J. Wu, Z. Wang, D. Zhao, *ACS Appl. Mater. Interfaces* **2020**, *12*, 53973.
[21] J. Ge, W. Li, X. He, H. Chen, W. Fang, X. Du, Y. Li, L. Zhao, *Mater. Today Energy* **2020**, *18*, 100562.
[22] a) B. Ahmed, D. H. Anjum, M. N. Hedhili, Y. Gogotsi, H. N. Alshareef, *Nanoscale* **2016**, *8*, 7580; b) J. Wang, Z. Cai, D. Lin, K. Chen, L. Zhao, F. Xie, R. Su, W. Xie, P. Liu, R. Zhu, *ACS Appl. Mater. Interfaces* **2021**, *13*, 32495.
[23] a) F. Yang, Y. Ge, T. Yin, J. Guo, F. Zhang, X. Tang, M. Qiu, W. Liang, N. Xu, C. Wang, Y. Song, S. Xu, S. Xiao, *ACS Appl. Nano Mater* **2020**, *3*, 11850; b) J. M. Powell, J. Adcock, S. Dai, G. M. Veith, C. A. Bridges, *RSC Adv.* **2015**, *5*, 88876.
[24] C. Liu, Y. Yang, O. A. Syzgantseva, Y. Ding, M. A. Syzgantseva, X. Zhang, A. M. Asiri, S. Dai, M. K. Nazeeruddin, *Adv. Mater.* **2020**, *32*, 2002632.
[25] J. Xue, R. Wang, K. L. Wang, Z. K. Wang, I. Yavuz, Y. Wang, Y. Yang, X. Gao, T. Huang, S. Nuryyeva, J. W. Lee, Y. Duan, L. S. Liao, R. Kaner, Y. Yang, *J. Am. Chem. Soc.* **2019**, *141*, 13948.
[26] a) S. Yuan, F. Qian, S. Yang, Y. Cai, Q. Wang, J. Sun, Z. Liu, S. Liu, *Adv. Funct. Mater.* **2019**, *29*, 1807850; b) Y. Cai, J. Cui, M. Chen, M. Zhang, Y. Han, F. Qian, H. Zhao, S. Yang, Z. Yang, H. Bian, T. Wang, K. Guo, M. Cai, S. Dai, Z. Liu, S. Liu, *Adv. Funct. Mater.* **2020**, *31*, 2005776.
[27] Z. Wu, M. Jiang, Z. Liu, A. Jamshaid, L. K. Ono, Y. Qi, *Adv. Energy Mater.* **2020**, *10*, 1903696.
[28] N. Li, S. Tao, Y. Chen, X. Niu, C. K. Onwudinanti, C. Hu, Z. Qiu, Z. Xu, G. Zheng, L. Wang, Y. Zhang, L. Li, H. Liu, Y. Lun, J. Hong, X. Wang, Y. Liu, H. Xie, Y. Gao, Y. Bai, S. Yang, G. Brocks, Q. Chen, H. Zhou, *Nat. Energy* **2019**, *4*, 408.
[29] a) H. Chen, T. Liu, P. Zhou, S. Li, J. Ren, H. He, J. Wang, N. Wang, S. Guo, *Adv. Mater.* **2020**, *32*, 1905661; b) S. Yang, H. Zhao, M. Wu, S. Yuan, Y. Han, Z. Liu, K. Guo, S. Liu, S. Yang, H. Zhao, S. Yuan, Y. Han, Z. Liu, S. Liu, M. Wu, K. Guo, *Sol. Energy Mater. Sol. Cells* **2019**, *201*, 110052.
[30] T. J. Macdonald, A. J. Clancy, W. Xu, Z. Jiang, C. T. Lin, L. Mohan, T. Du, D. D. Tune, L. Lanzetta, G. Min, T. Webb, A. Ashoka, R. Pandya, V. Tileli, M. A. McLachlan, J. R. Durrant, S. A. Haque, C. A. Howard, *J. Am. Chem. Soc.* **2021**, *143*, 21549.
[31] F. Qian, S. Yuan, Y. Cai, Y. Han, H. Zhao, J. Sun, Z. Liu, S. Liu, *Sol. RRL.* **2019**, *3*, 1900072.
[32] F. Li, J. Yuan, X. Ling, Y. Zhang, Y. Yang, S. H. Cheung, C. H. Y. Ho, X. Gao, W. Ma, *Adv. Funct. Mater.* **2018**, *28*, 1706377.
[33] a) J. Zhang, Y. Fang, W. Zhao, R. Han, J. Wen, S. F. Liu, *Adv. Mater.* **2021**, *33*, 2103770; b) W. Zhao, D. Yang, S. F. Liu, *Small* **2017**, *13*, 1604153; c) Z. Yao, W. Zhao, S. Chen, Z. Jin, S. F. Liu, *ACS Appl. Energy Mater.* **2020**, *3*, 5190.
[34] S. Yang, W. Liu, Y. Han, Z. Liu, W. Zhao, C. Duan, Y. Che, H. Gu, Y. Li, S. Liu, *Adv. Energy Mater.* **2020**, *10*, 2002882;
[35] Y. Zhang, J. Chen, X. Lian, M. Qin, J. Li, T. R. Andersen, X. Lu, G. Wu, H. Li, H. Chen, *Small Methods* **2019**, *3*, 1900375.
[36] C. Li, Z. Song, D. Zhao, C. Xiao, B. Subedi, N. Shrestha, M. M. Junda, C. Wang, C. S. Jiang, M. Al-Jassim, R. J. Ellingson, N. J. Podraza, K. Zhu, Y. Yan, *Adv. Energy Mater.* **2018**, *9*, 1803135.
[37] M. Lu, Z. Zhang, L. Kang, X. He, Q. Li, J. Sun, R. Jiang, H. Xu, F. Shi, Z. Lei, Z.-H. Liu, *J. Mater. Chem. A* **2019**, *7*, 12582.